

Experimentation at a muon collider

Massimo Casarsa,¹ Donatella Lucchesi² and Lorenzo Sestini³

¹INFN Sezione di Trieste, via Valerio 2, I-34127 Trieste, Italy; email: massimo.casarsa@ts.infn.it

²Department of Physics and Astronomy "G. Galilei" and INFN, via Marzolo 8, I-35131 Padova, Italy; email: donatella.lucchesi@pd.infn.it

³INFN Sezione di Padova, via Marzolo 8, I-35131 Padova, Italy; email: lorenzo.sestini@pd.infn.it

Xxxx. Xxx. Xxx. Yyyy. AA:1–28

<https://doi.org/10.1146/annurev-nucl-102622-011319>

Copyright © YYYY by the author(s).
All rights reserved

Keywords

muon collider, detector, multi-TeV muon collisions, Higgs boson, new physics

Abstract

Experimental activities involving multi-TeV muon collisions are a relatively recent endeavor. The community has limited experience in designing detectors for lepton interactions at center-of-mass energies of 10 TeV and beyond. This review provides a short overview of the machine characteristics and outlines potential sources of beam-induced background that could impact the detector performance.

The strategy for mitigating the effects of beam-induced background on the detector at $\sqrt{s} = 3$ TeV is discussed, focusing on the machine-detector interface, detector design, and the implementation of reconstruction algorithms.

The physics potential at this center-of-mass energy is evaluated using a detailed detector simulation that incorporates the effects of beam-induced background. This evaluation concerns the Higgs boson couplings and the Higgs field potential sensitivity, that then are used to get confidence on the expectations at 10 TeV.

The physics and detector requirements for an experiment at $\sqrt{s} = 10$ TeV, outlined here, form the foundation for the initial detector concept at that center-of-mass energy .

Contents

1. INTRODUCTION: YET ANOTHER COLLIDER?	2
1.1. Muon collider concept	2
1.2. The beauty of colliding muons	4
2. THE MUON COLLIDER SEEN FROM THE EXPERIMENTAL POINT OF VIEW	5
2.1. Background contributions in the detector region	5
2.2. Beam-induced background characteristics	6
3. DETECTOR PERFORMANCE IN THE PRESENCE OF THE BEAM-INDUCED BACKGROUND	7
3.1. Detector requirements and comparison with LHC experiments	8
3.2. Muon collider detector concept at $\sqrt{s} = 3$ TeV	9
3.3. Beam-induced background mitigation in the tracking system	11
3.4. Beam-induced background mitigation in the calorimeter system	12
3.5. Physics objects reconstruction with particle flow	14
3.6. Luminosity measurement	15
4. THE GUARANTEED PHYSICS DISCOVERY: FULL DETERMINATION OF THE HIGGS BOSON PROPERTIES	16
4.1. The Higgs boson couplings determination	18
4.2. The Higgs boson self-couplings and the Higgs potential	19
5. THE EXPERIMENT AT THE 10 TEV FRONTIER	20
5.1. Quest for new physics	21
5.2. Physics and detector requirements for an experiment at $\sqrt{s} = 10$ TeV	21
6. OUTLOOK	24

1. INTRODUCTION: YET ANOTHER COLLIDER?

A systematic study of multi-TeV muon collider started as a project in US in 2011 with the Muon Accelerator Program (MAP) (1, 2) to investigate the feasibility of a facility where both neutrino physics and experiments based on muon collisions could be possible. MAP designed colliders with center-of-mass energies of 1.5, 3, and 6 TeV¹ and optimized the interaction region (IR) configuration for a collider operating at $\sqrt{s} = 1.5$ TeV. After the recommendations of *The 2020 Update of the European Strategy for Particle Physics* (3), an International Muon Collider Collaboration (IMCC) (5) was formed currently hosted at CERN with the aim of establishing a feasible design and defining the necessary R&D for a multi-TeV muon collider. The Snowmass2021 process (4), a community planning exercise in particle physics, has strengthened the collaboration between US and Europe allowing to revise the studies performed by MAP and to progress in the design of the facility. The current focus is on the definition of the parameters of a muon collider at $\sqrt{s} = 3$ and $\sqrt{s} = 10$ TeV, but the project still foresees a facility where also neutrino experiments can be located.

1.1. Muon collider concept

The design of a muon collider facility is mainly driven by the short lifetime of muons, 2.2μ at rest. A conceptual layout of such a facility is presented in **Figure 1**. It foresees a muon

¹In this paper natural units where $\hbar = c = 1$ are used.

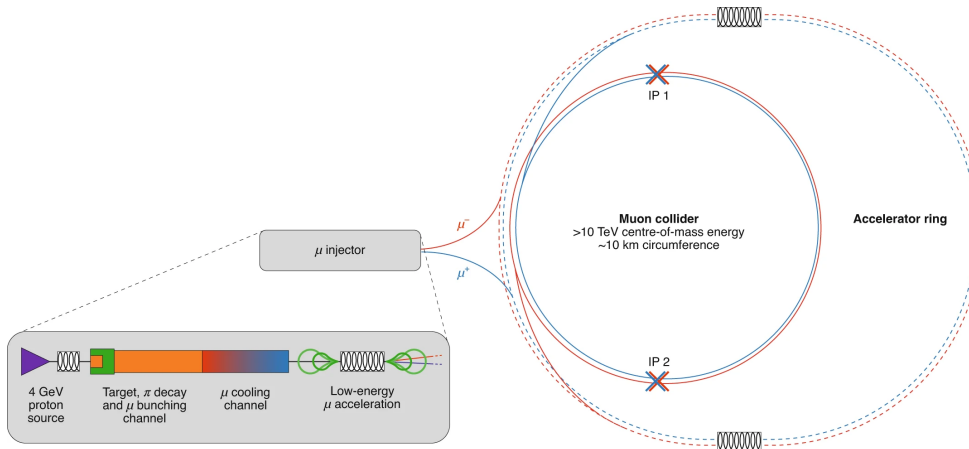


Figure 1

Conceptual layout of a multi-TeV muon collider.

injector and two rings, a large one for muon acceleration and a small one for collisions. The reduced dimensions of the collider are required to allow muons to pass through the interaction point many times before decaying. The current rings dimensions (6) do not consider any specific site, and by adjusting the machine configuration, they can potentially exploit existing and planned infrastructure at CERN and Fermilab. Preliminary parameters of the muon collider complex (6), relevant for what will follow, are summarized in **Table 1**. It must be noticed that the instantaneous luminosity increases significantly from $\sqrt{s} = 3$ TeV to $\sqrt{s} = 10$ TeV. As demonstrated in (6), it grows approximately with the square of the muon beam energy at fixed average bending magnetic field. This is a feature of the muon collider due to the fact that the beam can be recirculated many times through the interaction point (IP) thanks to the negligible effect of the beamstrahlung on the focusing achievable at the interaction point. The luminosity benefits also from having only one bunch of μ^+ and one of μ^- at the time in the collider ring.

Muon decays along the collider ring produce intense high energy neutrino fluxes that can generate hadronic and electromagnetic showers when interacting with the environment underground. In particular, in the straight sections of the machine, intense and very collimated fluxes of high energy neutrinos are produced. The effects at the Earth surface where they emerge, even hundreds of kilometers away from the collider complex, are under study to ensure that the impact on the environment is significantly below the legal limits and

Table 1 Preliminary muon collider parameters based on a revised MAP design.

Parameter	Unit of measure	Target value	
Center-of-mass energy (\sqrt{s})	TeV	3	10
Luminosity	$10^{34} \text{ cm}^{-2} \text{ s}^{-1}$	2	20
Collider circumference	km	4.5	10
Muons/bunch	10^{12}	2.2	1.8
Beta function at IP	mm	5	1.5

the ones of LHC. The complete determination of such effects is a multi-parameter problem: they depend on the machine center-of-mass energy, the collider configuration and the geological characteristics of the soil.

The heart of the facility is the muon injector. Intense protons beams, produced by a proton source, hit a multi-Watt class target to generate pions that eventually decay to muons. The target is immersed in a high solenoidal magnetic field to capture and guide pions into the decay channel, where muons are captured in a bunch train, with a time dependent acceleration due to their different energies.

Muon cooling process is critical to achieve the necessary beta function at IP (see **Table 1**) for the high luminosity at any center-of-mass energy. The challenge of the cooling process is the muon short lifetime, the cooling must take place more quickly than any of the cooling methods presently in use. A new technology, called “ionization cooling”, has been tested by the Muon Ionization Cooling Experiment (MICE) (7). The particle momentum is reduced through ionization energy loss in absorbers and replenished only in the beam direction through radio-frequency cavities. MICE experimentally demonstrated the first part, it measured an increase in the phase-space density of the beam, and the results agree with the simulations. The cooling in the direction of the beam and the re-acceleration of the particles have to be proven even though well predicted by the simulation tuned on MICE experimental results.

The first step toward a muon collider facility is the demonstration of the 6D cooling at low emittance and the re-acceleration of the muon beam through several cooling cells (8). This requires, as highlighted in (6):

- design, construction and integration of the cooling cell;
- a sufficiently intense proton beam that impinges on a target to produce pions, typically with a momentum range of 100–300 MeV, that in turn decay into muons having large transverse emittance;
- an upstream instrumentation system to measure the muon beam properties and then guide it to a certain number of cooling cells;
- a downstream instrumentation apparatus that measures the beam characteristics.

The design of this experimental demonstration with the relative instrumentation is part of the current activities of the IMCC. This muon beam facility could be hosted in any place where an adequate proton source is available. Such a facility could also host physics experiments as the muon beam dump (9) project. The proposed study of new gauge forces would require a beam with energy of the order of 100 GeV, in addition to the dedicated detector. The feasibility of this experiment will be assessed during the design phase of the demonstration facility.

1.2. The beauty of colliding muons

Muon collisions at high center-of-mass energies open a completely new physics scenario. A muon collider offers the possibility to reach high center-of-mass energy with high luminosity and also to perform high precision measurements thanks to the fact that muons are elementary particles.

The direct particle production can proceed via s -channel $\mu^+\mu^-$ annihilation, in which heavy particles of mass M can be produced with a kinematical threshold at $M = \sqrt{s}/2$. As pointed out in (10), states such as Z' , W' , heavy Higgses or other heavy particles

could be produced singly in association with soft/collinear vector boson like γ , Z^0 and W^\pm overcoming the kinematical limit. Comparisons between proton-proton and muon colliders production cross sections for $2 \rightarrow 2$ and $2 \rightarrow 1$ processes are studied (11, 12) by taking into account the differences of electroweak states and colored states to have insight of the most appropriate collider to explore the very high energy regime. Such a comparison is not trivial, because it can not represent the peculiarities of the two machines and the complexity of the data produced in the two very different environments.

Multi-TeV muon beams colliding at an energy which is much higher than the electroweak scale, ~ 100 GeV, have high probability to emit electroweak bosons. A summary of the theoretical investigations performed so far on the characteristics of such an emission is provided in (6), where it is also mentioned that the experimental observation of these phenomena and their comparison with the theoretical predictions is, by itself, a very interesting measurement. At the center-of-mass energies considered, the vector boson fusion (VBF) is the dominant production process and this is why the muon collider is often referred to as a “vector boson collider”. The production cross section of standard model (SM) processes via VBF are very high, see for example the Higgs cross sections reported in **Figure 7a**, that, combined with the high luminosity of the collider and the very low physics background contribution, allow precise SM tests in a completely unexplored energy regime. The precise knowledge of the SM processes at a multi-TeV energy scale gives the possibility to probe new physics indirectly extending the reaches given by the direct interactions.

2. THE MUON COLLIDER SEEN FROM THE EXPERIMENTAL POINT OF VIEW

The design of a detector able to operate and take data at a multi-TeV muon collider has to take into account not only the physics requirements, but also the IR conditions.

The machine-detector-interface (MDI) studies performed by MAP and recently by the IMCC indicate that the final focusing magnets cannot be located more than ± 6 meters from the IP not to degrade the instantaneous luminosity. **Figure 2a** shows the configuration of a possible IR, where the available space for the detector along the beam axis is a total 12 meters. The vertical dimension can be bigger, but it would not enhance the physics acceptance, particularly at very high center-of-mass energy where several relevant physics process occur forward respect to the beam line **Section 5**.

2.1. Background contributions in the detector region

Elementary particle collisions usually do not have secondary interactions beyond the primary one as seen in hadron-hadron collisions. Nevertheless, muon collider suffers from background coming from the machine, the main sources expected to contribute in the detector region at $\sqrt{s} = 3$ and 10 TeV are:

- a) **Muon decay:** intense muon beams of energies of 1.5 and 5 TeV decay producing positrons and electrons of several TeV and high energy photons from synchrotron radiation of energetic electrons and positrons in the collider magnetic fields. The majority of these particles directly reach the detector and may compromise any physics measurements. The MAP project proposed to insert two conical-shaped absorbers, referred to as nozzles (13), made of tungsten and covered with borated polyethylene, inside the detector along the beamline (**Figure 2**). This combination

is effective in absorbing high-energy particles and reducing their impact on the detector. This shielding structure modifies the characteristics of the background arriving on the detector as discussed in **Section 2.2**.

- b) **Incoherent e^+e^- production:** the production cross section of e^+e^- pairs in high energy muon beams has been calculated in (14) starting from the original formulation of Landau and Lifshitz (15). Such a background is synchronous with the beam collisions and is mainly produced along the beam direction. The MAP project evaluated the contribution of this source of background for beams of 750 GeV (16) and found it to be almost negligible. This is primarily because the production cross-section is suppressed at low muon energy, and the detector's magnetic field effectively traps e^+e^- pairs near the beam line. As the beam energy increases, the probability of incoherent positrons and electrons production rises. Consequently, a stronger magnetic field is required to confine these particles near the beam-line. This contribution to the background has not been studied yet, a preliminary evaluation suggests that at $\sqrt{s} = 10$ TeV, a solenoidal magnetic field of about 5 T in the detector can significantly reduce the flux of incoherent e^+e^- pairs reaching the detector. However, given the potential impact of these particles on the detector internal layers, it is essential to conduct a detailed simulation study.
- c) **Beam halo:** beam losses are unavoidable, but at the moment they are not considered among the background sources in the detector region. It is believed that an appropriately designed collimation system positioned upstream of IP can effectively reduce these losses to a manageable level.

2.2. Beam-induced background characteristics

The nozzles inserted around the IP absorb the high energy electrons and positrons generated by the muon decays, but are responsible for fluxes of particles that eventually arrive to the detector. Electrons, positrons and photons interacting with the tungsten material of the nozzles and the IR machine elements generate electromagnetic showers. In addition, hadronic particles, mainly neutrons with a minor contribution from charged hadrons, are generated through photonuclear interactions with the IR material, including the nozzles. The borated polyethylene cladding of the nozzles is designed to absorb neutrons, but it also produces high fluxes of photons, which contribute to background signals in the calorimeter system (**Section 3.4**). Muons instead are produced in the Bethe-Heitler process (17) by energetic photons from electromagnetic showers.

An assessment of the effects of the beam-induced background (BIB) on the detector response involves a laborious procedure. It must be noticed that BIB sample used in the detector studies until now was produced by MAP using the MARS15 software (18, 19) at a center-of-mass energy of 1.5 TeV. The IR and the nozzle dimensions and composition were optimized to minimize the occupancy on the first layers of the tracking system.

The IMCC has setup a software procedure to simulate the beam induced background (20):

- 1) IR accelerator lattice and optics are modeled in the FLUKA code (21) via the LineBuilder (22) package as well as the nozzles.
- 2) The detector solenoidal magnetic field is included in the IR description.

- 3) A primary beam is simulated starting from a given distance, L_{BIB} from the IP; the value of L_{BIB} depends on the center-of-mass energy and it is given by the point along the beam-line where the cumulative distribution of particles exiting the machine start saturating to 100%. Given the symmetric nature of μ^+/μ^- only one primary beam is considered.
- 4) Particles exiting the machine, either from the nozzles or from any of the IR components, are saved and then provided as an input to GEANT4 (23) simulation software to be tracked inside the detector.

The optimization path requires to execute all the actions from 1) to 4) with a given IR and nozzle configuration, evaluate the occupancy in the detector until an acceptable/optimal value is reached. The procedure has been executed by using $\sqrt{s} = 1.5$ TeV IR and the results compared with those obtained with MARS15 simulation code showing a very good agreement (20), giving robustness to the evaluation of the beam-induced background in the detector.

The determination of the characteristics of such a background at $\sqrt{s} = 3, 10$ TeV is in its early stage. The IR at a center-of mass energy of 3 TeV (24) comes from MAP, the preliminary design at $\sqrt{s} = 10$ TeV has been done by the IMCC (25). By using the nozzles proposed by MAP (13), the beam-induced background has been generated for both machine configurations. The solenoidal magnetic field is 3.57 T. **Figure 2b** shows the energy distributions of particles at $\sqrt{s} = 3$ TeV and $\sqrt{s} = 10$ TeV for each particle type arriving on the detector in a time window of $[-1, 15]$ ns with respect to the collision time (26). The two center-of-mass energies show a similar behavior, which is also similar to the one at $\sqrt{s} = 1.5$ TeV (6). Given the wide range of energies considered, this demonstrates that the energy distribution of the beam-induced background is determined by the nozzles. **Figure 2c** illustrates the particles arrival time on the detector still for the same center-of-mass energies. The distributions, similar in the two energies cases, show a sizeable contribution out of the time window considered as adequate for data taking. The similar behavior is expected due to the similar energy spectrum. It can be noticed that the absolute value at $\sqrt{s} = 10$ TeV is slightly higher than that at $\sqrt{s} = 3$ TeV, mainly for two reasons: the different center-of-mass energy and IR configuration. An important effort is ongoing to optimize the IR and the nozzles shape and materials for the center-of-mass energy of 3 and 10 TeV.

3. DETECTOR PERFORMANCE IN THE PRESENCE OF THE BEAM-INDUCED BACKGROUND

The design of an experiment at a multi-TeV muon collider has many features in common with the experiments at other proposed multi-TeV machines (27, 28, 29, 30), but also presents several novel challenges due to the unique background conditions related to the unstable nature of muons. The first constraints come from the machine layout and the detector shielding requirements. As discussed in **Section 2**, the available space around the interaction region is limited by the collider final focusing magnets and the MDI, in particular the nozzles reduce the angular acceptance in the forward and backward regions of the detector. In addition, each sub-detector must deal with the beam-induced background to ensure optimal physics performance.

In the following sections only one detector concept is discussed. Given that the muon collider can have two interaction points, different decisions can be made during the actual

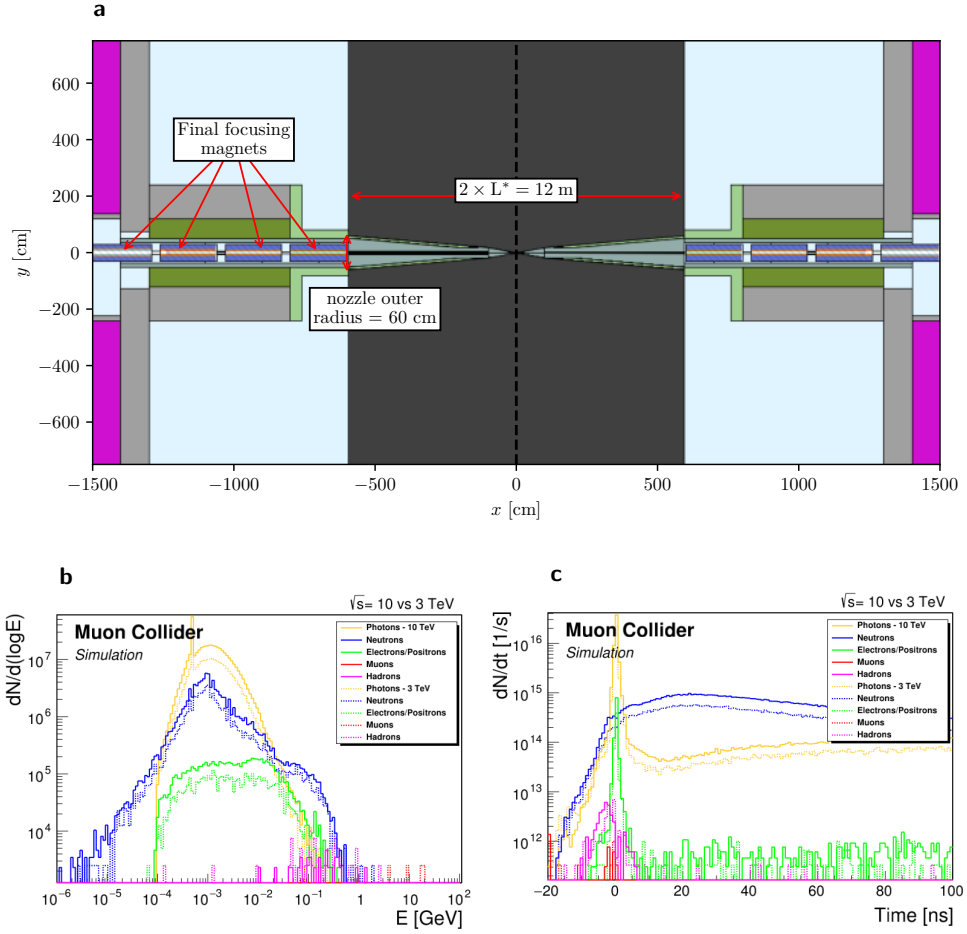


Figure 2

(a) Top view of the IR, the x axis represents the beam direction. The outer shape of the detector is a cylinder with a radius of 6 m. The space between the outer shape and the nozzles is considered as a perfect particle absorber. (b) Energy distribution of particles arriving at the detector for $\sqrt{s} = 3$ TeV (dashed line) and $\sqrt{s} = 10$ TeV (solid line). Different colors represent different types of particles. (c) Distribution of the arrival time of the various particle types for the two center-of-mass energies and with the same legend as used in figure (b).

design phase.

3.1. Detector requirements and comparison with LHC experiments

The presence of the BIB makes the detector requirements more similar to those for proton-proton than for positron-electron collisions. In addition, detector technology R&D is currently focused on the High Luminosity LHC (HL-LHC) (32), making it interesting to have LHC (31), with its experiments, and HL-LHC as references.

The starting point is the comparison of the beam dimensions at the muon collider with the nominal LHC configuration (33): the parameters at the interaction point are reported

in **Table 2**. At the IP, the bunch of the muon collider is shorter and narrower compared to

Table 2 Comparison of the beam size at IP for LHC and muon collider.

	LHC	muon collider	
\sqrt{s}	14 TeV	3 TeV	10 TeV
bunch length	7.7 cm	5 mm	1.5 mm
transversal bunch size	16.7 μm	3 μm	0.9 μm

that of the LHC. Consequently, the first detector layer can be positioned closer to the beam line with respect to the ATLAS (34) and CMS (35) detectors, to enhance the resolution on the impact parameter and the displaced vertices reconstruction. On the other hand, this is the region where the BIB flux is more intense, and large detector occupancies are expected. Another significant difference with respect to LHC is that the muon collider is expected to operate in single bunch mode and thus the bunch crossing rate coincides with the beam revolution frequency. This results in an expected bunch crossing rate below 100 kHz (with respect to 40 MHz at LHC) and implies a longer time between two collisions for processing and reading out the detector signals.

Similar to the upgraded ATLAS and CMS experiments for the HL-LHC, where it will be crucial to precisely measure time to disentangle the pile-up interactions, at the muon collider time measurements are necessary to mitigate the effects of the out-of-time BIB particles. For this purpose, sensors with time resolutions in the 30-100 ps range should be developed. It is clear that the R&D path towards such precise devices can benefit from synergies with the development of HL-LHC detectors.

Studies on the radiation environment due the BIB at $\sqrt{s} = 1.5$ TeV are documented in (11). **Table 3** presents the approximate expected radiation levels per year of data taking and compares them to HL-LHC estimates. Notably, the maximum total integrated dose is of about 10 Mrad in the region close to the interaction point (distance $R = 2.2$ cm), while at HL-LHC it is higher, around 100 Mrad. Conversely, the maximum fluence in the calorimeter region ($R = 150$ cm) is $\sim 10^{14}$ 1 MeV neutron equivalent per cm^2 at the muon collider, while it is $\sim 10^{13}$ 1 MeV neutron equivalent per cm^2 at the HL-LHC. Despite some differences in the radiation environment, similar radiation hardness requirements could be expected for the muon collider and the HL-LHC detectors.

Table 3 Radiation levels per year at a $\sqrt{s} = 1.5$ TeV muon collider and HL-LHC.

	muon collider	HL-LHC
maximum dose at $R = 2.2$ cm	10 Mrad	100 Mrad
maximum dose at $R = 150$ cm	0.1 Mrad	0.1 Mrad
maximum fluence at $R = 2.2$ cm	10^{15} 1 MeV-neq/ cm^2	10^{15} 1 MeV-neq/ cm^2
maximum fluence at $R = 150$ cm	10^{14} 1 MeV-neq/ cm^2	10^{13} 1 MeV-neq/ cm^2

3.2. Muon collider detector concept at $\sqrt{s} = 3$ TeV

The design of the first muon collider detector concept at $\sqrt{s} = 3$ TeV was based on CLIC detector (36), which had been optimized for e^+e^- collisions up to 3 TeV. However, modifications were necessary to adapt it to the muon collider MDI, described in **Section 2**, and

to mitigate the effects of the BIB.

The detector, illustrated in **Figure 3**, consists of a tracking system and a calorimeter system, both immersed in a uniform solenoidal magnetic field, with an external muon detector. From the innermost to the outermost regions with respect to the IP, it features the following components:

- **Vertex detector** made of double layers of $25 \times 25 \mu\text{m}^2$ silicon pixels. It features four central barrel cylinders and four endcap disks on both sides of the barrel.
- **Inner tracker** with three barrel layers and seven endcap disks on each side made of silicon macropixels with a size of $50 \mu\text{m} \times 1 \text{ mm}$.
- **Outer tracker** composed of three barrel layers and four endcap disks per side of silicon microstrips with a size of $50 \mu\text{m} \times 10 \text{ mm}$.
- **Electromagnetic calorimeter** (ECAL), composed of 40 alternating layers of tungsten absorber and silicon sensors as active material, for a total of 22 radiation lengths (X_0). The cell granularity is $5 \times 5 \text{ mm}^2$.
- **Hadronic calorimeter** (HCAL), that has 60 alternating layers of steel absorber and scintillating-pads active material, for a total of 7.5 interactions lengths (λ_I) and with cells of size $30 \times 30 \text{ mm}^2$.
- **Superconductive solenoid** generates a magnetic field of $B = 3.57 \text{ T}$; the magnetic field value has been chosen to be consistent with that used in the generation of the BIB sample.
- **Return yoke** equipped with resistive plate chambers (RPCs) for muon detection, with seven layers in the barrel and six layers in the endcap. Each cell has an area of $30 \times 30 \text{ mm}^2$.

The radius of the tracker barrel is 1.5 m, while the calorimeters barrel have outer radii of 1.7 m and 3.3 m, for ECAL and HCAL respectively. The total radial dimension of the detector, including the return yoke, is 6.5 m, and the detector length along the beam direction is $\pm 5.6 \text{ m}$ with respect to the IP.

In order to study the impact of BIB on the physics performance, the interactions of these particles with the detector are simulated using the muon collider software framework (37). This software is a branched version of iLCSoft (38), a framework developed for electron-positron colliders. The detector description is implemented with DD4hep (39) and the interaction of the BIB with the detector is simulated with GEANT4 (23). The BIB sample used to study the detector response was generated with MARS15 at $\sqrt{s} = 1.5 \text{ TeV}$. As discussed in **Section 2.2**, beam-induced background samples generated with FLUKA at $\sqrt{s} = 1.5$ and 3 TeV have become available only recently and show good compatibility. The particles produced by the primary muon-muon collisions (*i.e.* the physics signal) are generated with different programs like MadGraph5_aMC@NLO (41) or WHIZARD (40). The interactions of final state particles with the detector are then simulated with GEANT4. The digitization of the detector hits and the reconstruction of the physics object are performed by the Marlin software (42). Marlin also overlays the hits produced by the BIB particles onto the physics signal hits on an event-by-event basis.

By exploiting the detailed detector simulation, several strategies have been developed to mitigate the effects of BIB. Dedicated reconstruction algorithms have been employed to achieve high performance physics measurements. In the following sections, these techniques are described for the tracking and calorimeter systems (**Sections 3.3** and **3.4**, respectively). The discussion also covers the physics objects reconstruction performance achieved by com-

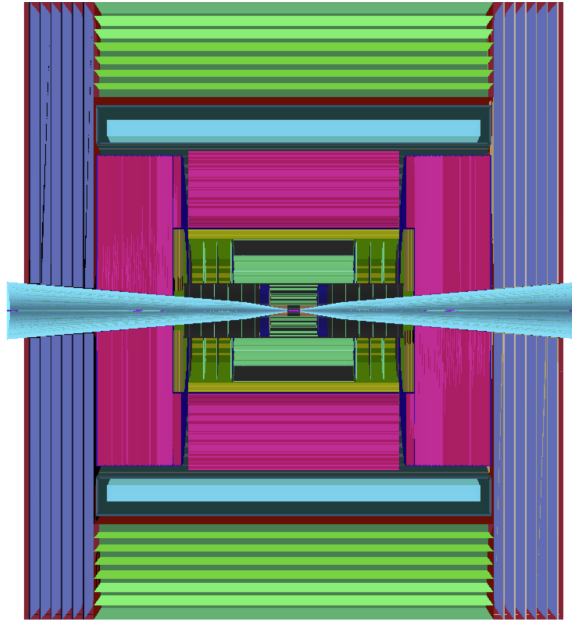


Figure 3

Muon collider detector concept. From the innermost to the outermost regions, it includes the tracking system (green), the electromagnetic calorimeter (yellow), the hadronic calorimeter (magenta), the superconducting solenoid (light blue), the barrel (light green) and endcap (blue) muon detectors. The nozzles are shown in cyan.

binning information from the different sub-detectors (**Section 3.5**).

3.3. Beam-induced background mitigation in the tracking system

The BIB is responsible for a high hit occupancy in the tracking system, especially in the first layers of the vertex detector. Hit densities of 3.68 mm^{-2} and 0.51 mm^{-2} are expected in the first and second pixel layers, respectively (6). These values are almost one order of magnitude higher than those predicted for the HL-LHC experiments. Nevertheless, it has to be remarked that the bunch crossing rate at muon collider is expected much lower than LHC allowing more time for data processing.

The primary strategies for mitigating the BIB in the tracking system include:

- Exploiting the hit times in the silicon sensors.
- Utilizing directional information of the incoming particles.
- Employing pulse shape analysis of the signal.
- Analyzing the shape of hit clusters.

As explained in **Section 2**, a significant fraction of the BIB is out-of-time with respect to the bunch crossing. Therefore, this component can be significantly reduced by requiring the hit times to be compatible with the timing of a particle coming from the IP. A time resolution of 30 ps is assumed for the vertex detector sensors, while a time resolution of 60

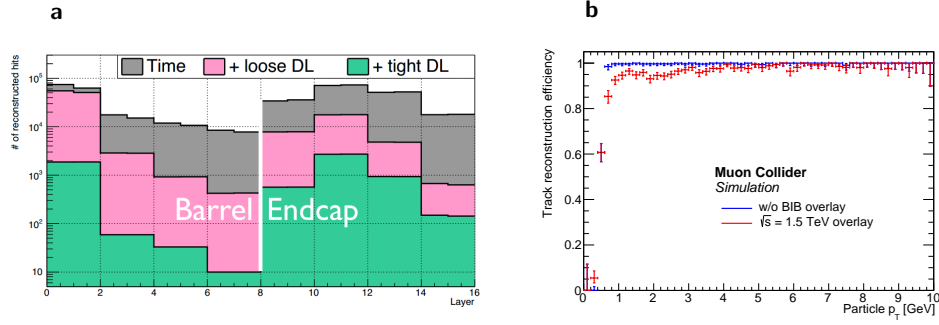


Figure 4

(a) Hit density as a function of the vertex detector layer, with the reduction obtained with time requirements and double layer (DL) filters. (b) Muon track reconstruction efficiencies as a function of the p_T , with and without the BIB overlaid (6).

p_T is considered for the inner and outer trackers.

Most of the BIB particles arriving at the detector originate far from the IP, so their incoming direction does not point directly to the interaction region. The double-layer configuration of the vertex detector can be exploited to estimate the direction of the particle by correlating the hit positions on adjacent layers. The effective hit occupancy reduction in the vertex detector, achieved by applying requirements on time and direction, is presented in **Figure 4a**. Notably, the hit density is reduced by more than an order of magnitude when using the double layer requirement. A further reduction can be achieved by considering the pulse shape at the sensor level and the shape of the hit clusters, but these studies are ongoing.

The hits that survive the BIB suppression are then utilized as input for the track reconstruction procedure. The primary algorithm employed for this purpose makes use of the Combinatorial Kalman Filter, often referred to as the CKF algorithm (43). This algorithm reconstructs the trajectory of charged particles in the magnetic field (tracks), allowing the measurement of their transverse momentum (p_T). The tracking algorithm was tested on samples of muons generated at the primary vertex. **Figure 4b** shows the track reconstruction efficiency as a function of muon p_T . To understand the impact of the BIB, these efficiencies are compared with those obtained without the BIB overlay. It is evident that the BIB leads to a drop in efficiency at low p_T , below 4 GeV, while the tracking efficiency remains close to 1 for muons with higher p_T . The estimated uncertainty on the transverse momentum is $\Delta p_T/p_T^2 \approx 1 \cdot 10^{-1}$ ($5 \cdot 10^{-3}$) GeV^{-1} for muons with momentum $p = 1$ (100) GeV and $\theta = 13^\circ$, and $\Delta p_T/p_T^2 \approx 5 \cdot 10^{-2}$ ($4 \cdot 10^{-5}$) GeV^{-1} for muons with $p = 1$ (100) GeV and $\theta = 89^\circ$ (6).

3.4. Beam-induced background mitigation in the calorimeter system

At the muon collider, the internal surface of the electromagnetic calorimeter (ECAL) is exposed to a flux of about 300 BIB particles per cm^2 at each bunch crossing. The majority of these particles are photons (96%) with an average energy of 1.7 MeV and the remaining 4% are neutrons. Neutrons that don't interact with the ECAL reach the HCAL where on the first layer, the occupancy is approximately one order of magnitude lower than that of the first ECAL layer (6). The following features can be exploited to suppress the BIB in

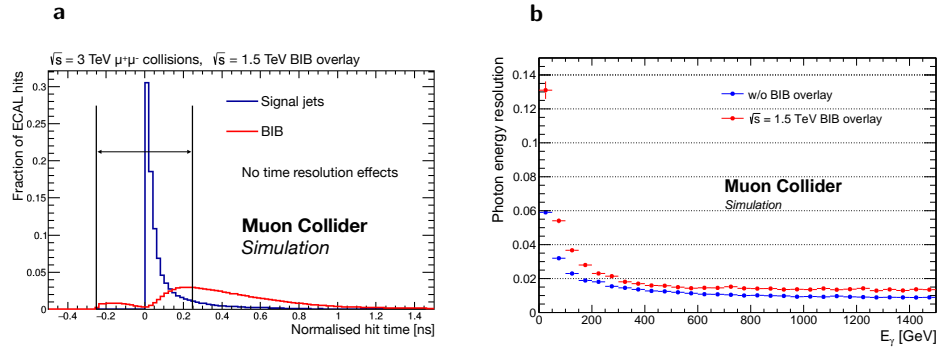


Figure 5

(a) Distribution of the ECAL hit times with respect to the bunch crossing for signal (hadronic jets) and BIB particles. (b) Photon energy resolution for low- and high-energy photons, obtained with and without the BIB overlaid (6).

the calorimeter:

- Arrival time of the particles in the calorimeter cells.
- Calorimeter granularity.
- Energy thresholds to reject the soft component.
- Calorimeter segmentation for the measurement of the longitudinal energy distribution.

Similarly to the tracking system, time information plays an important role also in the calorimeters. As shown in **Figure 5a**, the times of a consistent fraction of the BIB hits of the ECAL is out of the time window of the physics signal (*e.g.* hadronic jets). Assuming a calorimeter hit time resolution of approximately 100 ps, it is possible to apply a time window requirement of ± 250 ps, which efficiently suppresses a significant portion of BIB hits.

A high granularity and a fine longitudinal segmentation of the calorimeter could help in separating the showers initiated by signal particles from those due to the BIB. This is the reason why cells of $5 \times 5 \text{ mm}^2$ are considered for ECAL.

To suppress the low energy deposits associated with the BIB, a threshold of 2 MeV is set on the energy of the calorimeter cells. This threshold, while relatively high, represents a compromise between performance, BIB suppression and computation time. Nonetheless, new handles can be explored in the future to lower this threshold and enhance performance. For instance, the analysis of the longitudinal distribution of the deposited energy in the calorimeter can be leveraged to differentiate signal from BIB showers, as distinct profiles are expected.

The photon energy resolution achieved with the current calorimeter configuration and the aforementioned requirements is presented in **Figure 5b**. The resolution is approximately 13% for low energy photons below 50 GeV, and around 1.5% for photons with energy above 400 GeV. By comparing the resolution with that obtained without the BIB overlaid, it becomes evident that the BIB leads to a degradation in performance.

3.5. Physics objects reconstruction with particle flow

Several physics objects are crucial for the success of the muon collider physics program. The reconstruction and identification of muons, photons, electrons and jets have been studied with the detailed detector simulation. As explained in the following sections, these particles are present in the final states of the most important Higgs decay channels and may be part of the signatures for new physics searches.

The reconstruction of these physical objects involves combining information from all the detector sub-systems. Tracks, calorimeter clusters, and muon detector hits are combined to achieve optimal performance in terms of identification efficiency, background rejection, and momentum resolution. For this purpose, a particle flow algorithm, PandoraPFA (44), is employed. PandoraPFA is an algorithm based on modern particle flow techniques and has been used for object reconstruction tasks. Initial studies have demonstrated its effectiveness in the muon collider environment, although its initial configuration was optimized for electron-positron colliders. It is evident that there is room for further improvements and, in the future, a dedicated optimization of the PandoraPFA settings for the muon collider can be pursued.

The reconstruction of the following physics objects have been studied, along with the resulting performance:

- **Muons** are identified by matching tracks with hits in the muon detector system. This sub-detector is not significantly affected by the BIB, except for the forward region with respect to the beam direction. In **Figure 6a** the muon reconstruction and identification efficiency is presented as a function of the muon production angle with respect to the beamline. It is evident that the low angle region suffers from the BIB presence while the central region exhibits high efficiency.
- **Electrons** and **photons** are reconstructed by matching tracks with ECAL clusters. Isolated clusters are classified as photons, while clusters matched with a track are classified as electrons. The energy of electrons and photons is corrected to take into account inefficiencies and radiation losses. The electron reconstruction efficiency as a function of the energy is presented in **Figure 6b**: it reaches around 95% for high energy, but the typical efficiency drop at low energy caused by the BIB is evident.
- **Hadronic jets**: particles reconstructed by PandoraPFA are given in input to the jet clustering algorithm, that groups together particles belonging to the same fragmentation process, by exploiting their correlations. The jet algorithm used is the k_t algorithm (45, 46) with a radius parameter of 0.5. The resulting jet energy is corrected to recover the losses due to particles escaping the detector, detector inefficiencies, and also for the BIB contamination. The jet reconstruction algorithm has been tested with simulated samples of different jet flavours: gluons and b , c , u , d , and s quarks. The reconstruction efficiencies are illustrated in **Figure 6c**. Despite the presence of BIB throughout the detector, the efficiency ranges between 80% and 95%, with a negligible fake jet probability.
- **Heavy flavour jets**: in order to identify the jets originating from heavy quarks, secondary vertices compatible with the decays of b - and c -hadrons are reconstructed by combining tracks. A jet is identified as a heavy-flavour jet if one of these secondary vertices is reconstructed within the jet cone. The b -jet identification probability, called b -tagging efficiency, is shown in **Figure 6d**. It is of approximately 45% at low p_T (20 GeV) and increases to 70% at 120 GeV. This level of performance is comparable to

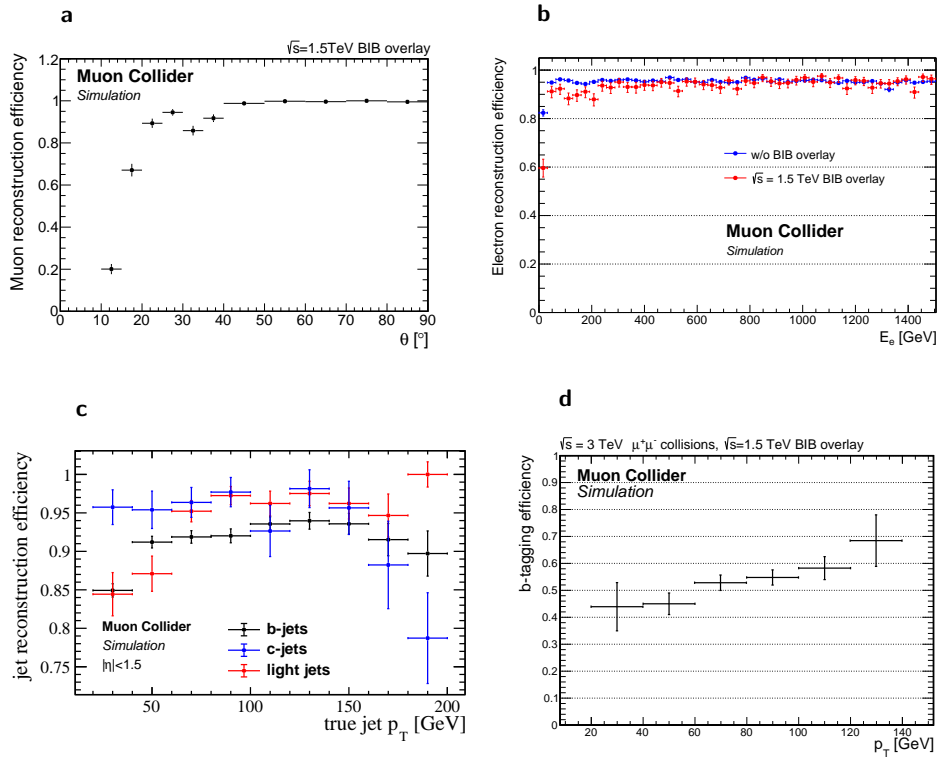


Figure 6

(a) Muon reconstruction efficiency as a function muon p_T . (b) Electron reconstruction efficiency as a function of the electron energy, with and without the BIB overlay. (c) Jet reconstruction efficiency as a function of jet p_T , for different jet flavours. (d) b -tagging probability as a function of the jet p_T . The above figures have been reproduced from (6).

what is currently achieved at hadron colliders. At lepton colliders, a higher efficiency is expected. The current algorithm is mainly limited by the presence of the BIB. In the future, artificial-intelligence-based methods will be implemented to minimize the effects of BIB and further enhance efficiency.

3.6. Luminosity measurement

Accurate knowledge of the absolute luminosity is crucial in collider experiments, as it is essential for determining the production cross sections. Uncertainty below 1% has been achieved by the ATLAS (48) and BelleII (49) experiments. In general, the luminosity measurement methods rely on the direct proportionality between process rates observed in the detector and luminosity. Two different approaches are typically used for hadron and lepton colliders:

- At hadron colliders, the rate R of a given process is measured and related to the integrated luminosity by $\mathcal{L}_{int} = R/\sigma_{vis}$. The visible cross section σ_{vis} is defined as $\sigma_{vis} = 2\pi A_{eff}/(N_1 N_2)$, where $N_{1,2}$ is the average number of particles per bunch

provided by the machine and A_{eff} is the effective transverse area of the luminous region. In this method, a precise calibration of the visible cross section is crucial. At the LHC, it is achieved with dedicated van der Meer scans (50), in which the beams are displaced against each other.

- Experiments at lepton colliders count the number of events N_{ev} of a reference process, whose cross section σ is sufficiently high and theoretically known with very good precision, and determine the luminosity by $\mathcal{L}_{int} = N_{ev}/(\epsilon\sigma)$, where ϵ is the total selection efficiency for the considered events. Electron-positron experiments exploit the abundant $e^+e^- \rightarrow e^+e^-$ elastic scattering (Bhabha scattering), for which the cross section is known with a precision below a percent at $\sqrt{s} = 1\text{-}10$ GeV (51).

In both cases, the rate of the reference processes is measured by dedicated detectors, called luminometers, that are installed at very small polar angles on both sides of the interaction point, where the observed rates are higher. In a muon collider experiment, the presence of the nozzles hinders the installation of the luminometers and an alternative technique must be utilized to determine the luminosity. A possible approach could be to count muons scattered elastically at large angles, similar to what was done in (54).

A preliminary study verified the feasibility of such a method (52). The Pythia Monte Carlo generator (53) was used to produce a sample of $\mu^+\mu^- \rightarrow \mu^+\mu^-$ Bhabha events with an emission angle of $30^\circ < \theta_\mu < 150^\circ$ with respect to the beam direction at a center-of-mass energy of 1.5 TeV. The sample was processed with the detector simulation and the muon collider reconstruction software. The event requirements are quite simple: two opposite-charge muons with a transverse momentum $p_T > 130$ GeV and an invariant mass $1440 < m_{\mu\mu} < 1560$ GeV. Background contributions from other physics processes are found to be negligible as well as possible effects from the beam-induced background. The statistical uncertainty on the integrated luminosity estimated at $\sqrt{s} = 1.5$ TeV is:

$$\frac{\Delta N_{Bhabha}}{N_{Bhabha}} = \frac{1}{\sqrt{N_{Bhabha}}} = 0.002 . \quad 1.$$

This approach requires the knowledge of the cross section of the μ -Bhabha scattering at large angles and a center-of-mass energy of several TeV, which is currently not available. Assuming this, the method seems promising.

4. THE GUARANTEED PHYSICS DISCOVERY: FULL DETERMINATION OF THE HIGGS BOSON PROPERTIES

The Higgs boson plays a fundamental role in the standard model and could hold the key to a deeper understanding of the universe. Its observation has been the key step in establishing the mechanism of electroweak symmetry breaking and mass generation (55). Precisely determining the Higgs boson properties and understanding its nature are therefore of the utmost importance in the particle physics field and are central to the physics programs of all the proposed next-generation colliders.

A high energy muon collider represents an ideal machine to study in detail the Higgs boson properties, since it is expected to provide large samples of single Higgs bosons as well as unprecedented samples of multi-Higgs bosons in a relatively clean experimental environment. The cross sections of the most important production channels are shown in **Figure 7a** as a function of the muon collider center-of-mass energy \sqrt{s} . At multi-TeV

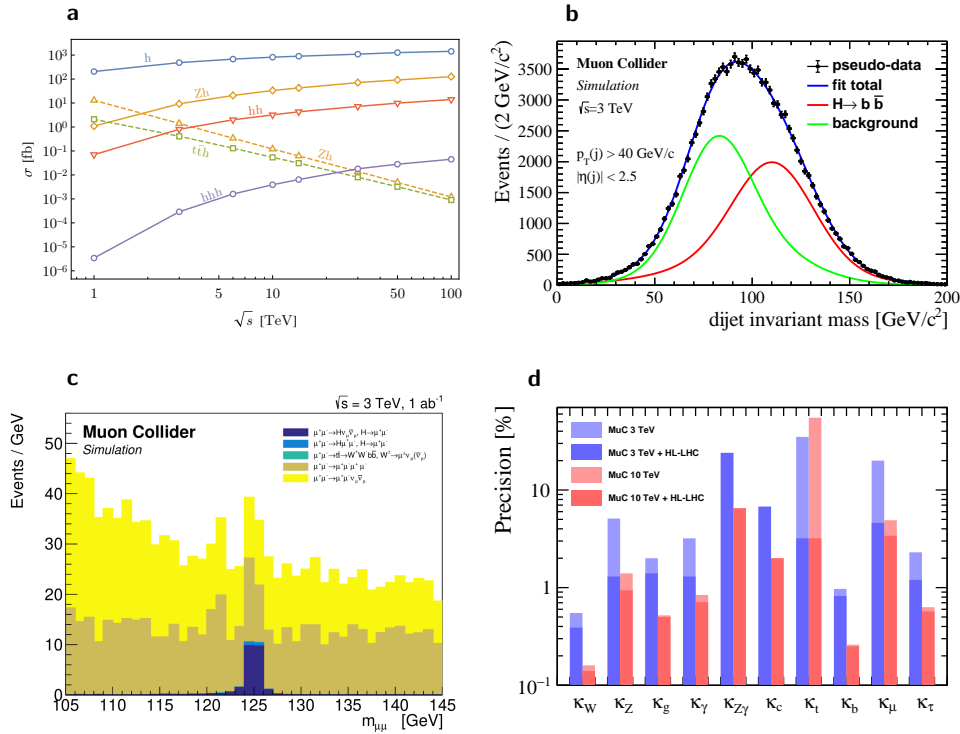


Figure 7

(a) Cross sections of the main Higgs boson production channels as a function of the muon collider center-of-mass energy \sqrt{s} , from Ref. (56). (b) Invariant mass of the two jets reconstructed in the $H \rightarrow b\bar{b}$ channel: the reconstructed mass peak of the Higgs boson is indicated in red, while the background is in green. (c) Invariant mass of the two muons in the $H \rightarrow \mu^+\mu^-$ analysis: the backgrounds (in yellow and brown) are stacked on top of the signal (dark blue). (d) Precision on the Higgs boson couplings at a 3 TeV and 10 TeV muon collider, with a dataset of 1 ab^{-1} and 10 ab^{-1} , respectively. The light-colored histograms indicate the expected precision of muon collider alone, while the dark-colored ones show the precision when combining with the HL-LHC. The plotted values are taken from (64).

lepton collisions, Higgs bosons are produced via two fundamental processes: the vector boson fusion and the muon-antimuon annihilation. The cross sections of the latter decrease as $1/s$ with increasing collision energies, whereas the former displays cross sections that increase logarithmically with s and eventually become dominant at high energies.

A 3 TeV muon collider with a dataset of 1 ab^{-1} is expected to produce a sample of approximately 5.5×10^5 single Higgs bosons and a sample of about 1000 double Higgs events. A muon collider operating at 3 TeV would undoubtedly advance our understanding of the Higgs boson's properties significantly, but it is at higher energies that the full potential of a muon collider emerges. At a 10 TeV collider with a dataset of 10 ab^{-1} , approximately 9.3 million of single Higgs bosons and a sample of about 38000 double-Higgs events are expected. The 1 ab^{-1} and 10 ab^{-1} datasets correspond to the integrated luminosity targets set in the IMCC's studies (6).

4.1. The Higgs boson couplings determination

A first campaign of studies to estimate the precision on the Higgs cross sections in different final states was carried out at $\sqrt{s} = 3$ TeV with a detailed detector simulation that includes the beam-induced background. Given the unique nature of such a background, it was not possible to model or parameterize its impact on the detector performance, and hence the physics reach, relying on prior experience with machine backgrounds at current or past colliders.

The physics objects described in **Section 3.5** were used to reconstruct the Higgs boson decays into the final states $f = b\bar{b}$, WW^* , ZZ^* , $\gamma\gamma$, and $\mu^+\mu^-$ to estimate the statistical sensitivity on the production cross sections multiplied by the decay branching ratios: $\sigma_H \times BR(H \rightarrow f)$.

The Higgs and physics background samples were generated at leading order with WHIZARD or MadGraph5_aMC@NLO and Pythia8 was used for the final state hadronization. The samples were then processed with the detailed detector simulation and reconstructed with the muon collider software. The results are outlined below. A dataset of 1 ab^{-1} and a single interaction point are assumed. A natural reference to compare to are the corresponding results by CLIC at $\sqrt{s} = 3$ TeV (57) with the caveat that CLIC is assuming a dataset of 2 ab^{-1} and the number of reconstructed final states for each Higgs boson decay mode are in some cases different.

$H \rightarrow b\bar{b}$: The $b\bar{b}$ channel (58) is reconstructed selecting two central high- p_T jets satisfying: $p_T^{\text{jet}} > 40 \text{ GeV}$ and $|\eta_{\text{jet}}| < 2.5$. Once the b -flavor identification is applied to both jets the only significant background that survives is from Z^0 boson decays into $b\bar{b}$ and $c\bar{c}$ pairs. A total number of 59500 signal events and 65400 background events are estimated. **Figure 7b** shows the reconstructed dijet invariant mass. The dijet mass resolution is critical to separate the H and Z^0 peaks. The current value of the Higgs boson mass resolution is of about 18%, being dominated by BIB effects, *i.e.* the energy thresholds set on the calorimeter hits (see **Section 3.4**). The estimated sensitivity on $\sigma_H \times BR(H \rightarrow b\bar{b})$ is 0.75%, to be compared with 0.3% of CLIC.

$H \rightarrow WW^*$: The WW channel (59) is reconstructed in the semileptonic final state $qq'\mu\nu_\mu$, which provides a good signal-to-background ratio. Events are selected with at least two reconstructed jets, having $p_T^{\text{jet}} > 20 \text{ GeV}$ and $|\eta_{\text{jet}}| < 2.5$, and one muon with $p_T^\mu > 10 \text{ GeV}$ and $10^\circ < \theta_\mu < 170^\circ$. The estimated number of Higgs candidates is 2430 over a background of 2600 events. The resulting statistical uncertainty on the production cross section is 2.9%. Reconstructing the full hadronic channel and the semileptonic channels with both muons and electrons, CLIC achieves a sensitivity of 0.7%.

$H \rightarrow ZZ^*$: The ZZ^* channel (60) is reconstructed in the semileptonic final state $q\bar{q}\mu^+\mu^-$. Events are selected with at least two reconstructed jets and two opposite-charge muons, having $p_T^{\text{jet}} > 15 \text{ GeV}$ and $30^\circ < \theta_{\text{jet}} < 150^\circ$, $p_T^\mu > 10 \text{ GeV}$ and $10^\circ < \theta_\mu < 170^\circ$. The sensitivity estimated on the cross section with 55 signal events and 39 background events is 17%. CLIC analyses also the semileptonic channel with electrons and gets 3.9%.

$H \rightarrow \gamma\gamma$: The $\gamma\gamma$ analysis (61) searches for events with at least two reconstructed photons, featuring $E_\gamma > 15 \text{ GeV}$, $p_T^\gamma > 10 \text{ GeV}$ and $10^\circ < \theta_\gamma < 170^\circ$. The reconstruction of high energy photons is not significantly affected by the BIB. In fact, the diphoton

invariant mass exhibits a very good resolution of 3.2 GeV. The estimated numbers of signal and background events are 396 and 484, respectively, which result in a relative uncertainty on the production cross section of 7.6%, to be compared with CLIC's 10%.

$H \rightarrow \mu^+ \mu^-$: The $\mu\mu$ channel (62) is reconstructed selecting events with two opposite-charge muons in the kinematical region $p_T^\mu > 5$ GeV and $10^\circ < \theta_\mu < 170^\circ$. The BIB impact on the reconstruction of muons is found to be negligible. The reconstructed dimuon mass is shown in **Figure 7c**, where the signal peak has a width of 0.4 GeV. After the final selection, 26 signal events and 1114 background events are left, which result in a sensitivity on the production cross section of 38%. For this specific channel, CLIC's ability to veto events with electrons scattered at very low angles significantly reduces background contamination, resulting in a sensitivity of 25%.

A precise measurement of the the observables $\sigma_H \times BR(H \rightarrow f)$ reflects into a precise determination of the Higgs couplings to f , where f represents each standard model boson and fermion. The precision achievable on the couplings is usually estimated with a fit to the cross sections within the so-called κ -framework² (63). The studies carried out so far at the muon collider do not cover all the most relevant decay modes of the Higgs boson, mainly due to a lack of personnel; therefore, the coupling fit is not yet meaningful. Nonetheless, this exercise was extremely useful as it allowed to benchmark parametric studies with which it is possible to estimate the sensitivity on the Higgs couplings of an experiment at the muon collider at $\sqrt{s} = 3$ TeV. In fact, the parametric study in (64) presents results for the Higgs boson production cross sections consistent with those for the available channels with the detailed simulation. In the same study, it is shown how the identification of the Higgs production mechanism, WW or $Z^0 Z^0$ fusion, could help in improving the coupling sensitivity. However, this could be done mainly through the identification of the forward muons emitted outside the detector acceptance. Prospects on their detection are discussed in **Section 5.2.3**. The output of the fit of the couplings is reported in **Figure 7d** in the κ -framework for a muon collider of 3 TeV (1 ab^{-1}) and 10 TeV (10 ab^{-1}) independently and in combination with the HL-LHC estimates, in the assumption that there are no BSM decays of the Higgs boson. While the HL-LHC results are complementary to those of a 3 TeV muon collider, in the 10 TeV scenario the combination is definitely dominated by the muon collider precision, with the only exception of the top quark coupling.

4.2. The Higgs boson self-couplings and the Higgs potential

One of the strengths of the muon collider physics program is the possibility to determine the Higgs field potential. In the standard model (55), its configuration is parameterized in terms of the vacuum expectation value of the Higgs field $v = 1/\sqrt{\sqrt{2} G_F} = 246$ GeV, with G_F the Fermi constant, the strength of the Higgs self-coupling λ , and the Higgs boson mass $m_H = \sqrt{2\lambda} v$. Processes in which a virtual Higgs boson produces two or three Higgs bosons, governed by the so-called trilinear and quartic Higgs self-coupling, are of the utmost important to test whether the Higgs potential is consistent with that predicted by the standard model. To be as general as possible and to account for deviations from the

²The parameters κ_i are coupling modifiers, defined as the ratio between the measured and the standard model values.

standard model, the Higgs potential is formulated with two different values for trilinear (λ_3) and quartic (λ_4) self-couplings:

$$V(h) = \frac{1}{2}m_H^2 h^2 + \lambda_3 v h^3 + \frac{1}{4}\lambda_4 h^4, \quad 2.$$

where $\lambda_3 = \lambda_4 = \lambda = m_h^2/2v^2$ in the standard model and the scalar field, h , is an expansion around $v/\sqrt{2}$, describes a physical Higgs boson.

The gateway to the trilinear self-coupling is the double Higgs production cross section. Its measurement was studied with the detailed detector simulation in the hadronic final state $HH \rightarrow b\bar{b}b\bar{b}$ for a 3 TeV collider with an integrated luminosity of 1 ab^{-1} (58). Events are selected with at least four reconstructed jets having $p_T^{\text{jet}} > 20 \text{ GeV}$. The requirement of b -tagging suppresses most of the backgrounds from light quarks. A final number of 77 signal events and 1422 background events is expected, which leads to an estimated sensitivity on the production cross section of 33%. Including additional final states and assuming an 80% polarization of the electron beam, CLIC quotes a precision of 22% with 2 ab^{-1} of data. From this study, a preliminary estimate in the order of 20-30% is derived on the sensitivity on the trilinear self-coupling (60). It will be possible to determine the final sensitivity with the detailed detector simulation once all the relevant final states are included and the reconstruction algorithms, particularly the b -jet tagging, are fully optimized.

Since the design of the detector at $\sqrt{s} = 10 \text{ TeV}$ is not ready yet, a study by using a parametric description of the physics objects is performed. In (65) the sensitivity at 3 TeV center-of-mass energy has been evaluated with selections that mimic those applied in the analysis with the detailed simulation. The uncertainty on the trilinear self-coupling is around 25%. The exercise is repeated at 10 TeV center-of-mass energy finding an uncertainty of 5.6% assuming 10 ab^{-1} of data.

The muon collider offers a unique opportunity to measure the quartic self-coupling. A parametric study indicate that the quartic self-coupling can be probed to an accuracy of tens of percent (66) with 20 ab^{-1} of data. Here no background has been considered. The reconstruction of events with 6 jets, some of them in the forward region will require dedicated algorithms. In addition, at the moment the generation of the background with 6 b -jets final state is not viable due to high computational time required.

5. THE EXPERIMENT AT THE 10 TEV FRONTIER

The discovery potential of the multi-TeV muon collider can be exploited by looking for a large variety of signatures (6). The possibility of having collisions at $\sqrt{s} = 10 \text{ TeV}$ and beyond enables the search for new particles at an energy scale not accessible by other proposed e^+e^- colliders.

Although the importance of exploring high-mass particles is evident, the capability to measure low-momentum signatures should not be overlooked. As an example, scenarios with Higgs composite models or where dark matter is a particle charged under the electroweak interaction could be probed at the muon collider in a wide range of final state momenta. As will be discussed in this Section, the standard model Higgs physics can be considered low momentum physics at $\sqrt{s} = 10 \text{ TeV}$, as well as various other standard model measurements. The measurements done at $\sqrt{s} = 3 \text{ TeV}$ could be used to improve the LHC exclusion bounds for several models (67) and to perform precision standard model physics tests. Nevertheless, the muon collider potential will be fully unleashed with very high energy collisions.

5.1. Quest for new physics

As previously noted, muon collisions at $\sqrt{s} = 10$ TeV or higher offer an opportunity to investigate new physics scenarios at the energy frontier and to test several beyond standard model hypotheses. An experimental access to the signatures of many of these scenarios is closely tied to specific capabilities of the experimental apparatus. Below, such a connection is illustrated for some representative physics cases.

An overview of dark matter candidates that can be searched for at a $\sqrt{s} = 10$ muon collider can be found in (75). Within the framework of weakly interacting massive particles, this study demonstrates that an experiment at a muon collider has the potential to explore models where new electroweak particles are created in the early universe. This analysis is based on inclusive experimental signatures such as mono-photon, mono-muon, and dimuon events. A study performed with a detailed detector simulation of mono-photon signatures for searches related to axion-like particles (76) demonstrates the critical importance of detecting objects such as photons with energies in the TeV range. This is crucial for advancing the understanding of new physics, in particular the dark matter candidates.

New physics scenarios could manifest themselves with unconventional experimental signatures including, but are not limited to, long-lived particles, disappearing tracks, and emerging jets.

Disappearing tracks refer to charged long-lived particles that travel a few centimeters in the detector before decaying into undetectable particles, resulting in track stubs that do not traverse the entire tracker. The spurious hits produced by the beam-induced background in the tracker can potentially compromise the identification of this type of signatures.

The study presented in (73) demonstrates that the BIB can be effectively mitigated with an appropriate detector configuration and analysis strategy.

This study has been performed using the detector concept presented in **Section 3**. Further optimization aimed specifically at the 10 TeV center-of-mass energy configuration could improve the results.

The physics possibilities at a $\sqrt{s} \geq 10$ TeV muon collider extend beyond Higgs presented in **Section 4** and exotic signatures. The fact that vector bosons collisions dominate the inclusive $\mu^+\mu^-$ interactions at these energies results in unprecedented precise measurements of electroweak processes thanks to their high production cross section and the relatively clean environment. This offers a mean for indirectly probing new physics by identifying any deviations from the SM predictions. Measurements of vector boson scattering, the anomalous muon magnetic moment, b -hadron decays, and other possibilities can be explored in this context (6). Further studies based on detailed detector simulations will be necessary in the future to determine the optimal detector configuration and performance for this types of measurements.

5.2. Physics and detector requirements for an experiment at $\sqrt{s} = 10$ TeV

The detector design for an experiment at a muon collider at $\sqrt{s} = 10$ TeV is currently under study. In this section, requirements are discussed and guidelines are drawn, but further studies with the detailed simulation are necessary to validate the detector concept at $\sqrt{s} = 10$ TeV. This includes assessing the BIB at detector level, utilizing the $\sqrt{s} = 10$ TeV generation described in **Section 2.2**.

The detector design must aim to provide as much as possible good efficiencies and precision for new physics signatures from low to high momentum, conventional and uncon-

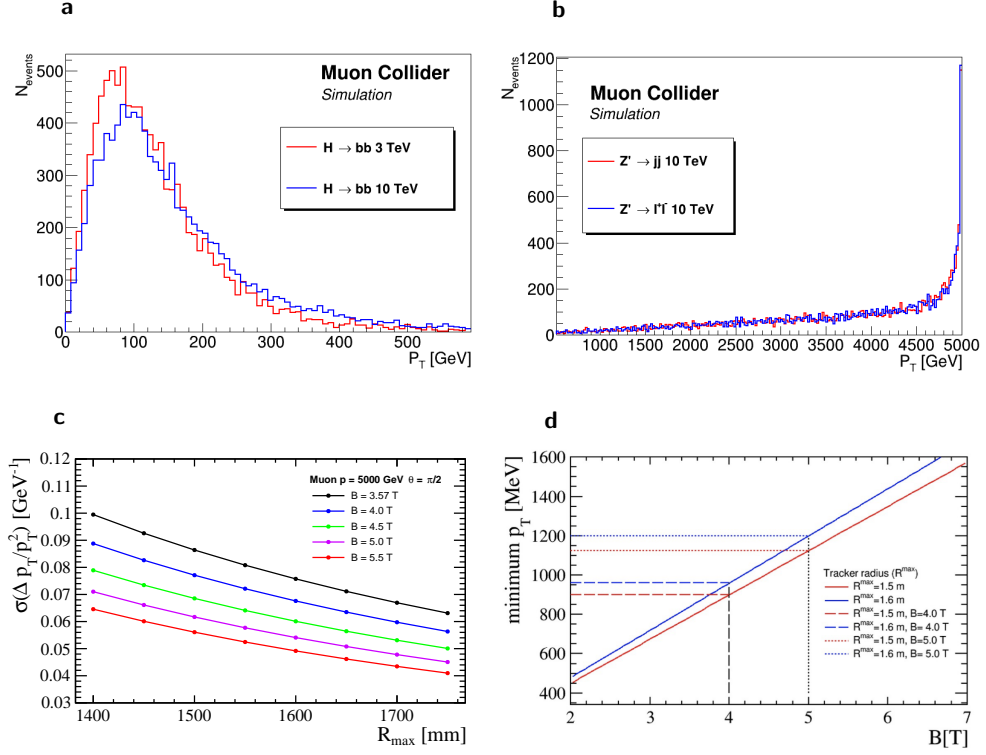


Figure 8

(a) b -quark p_T distributions from the $H \rightarrow b\bar{b}$ decays at $\sqrt{s} = 3$ and 10 TeV, as obtained at generator level. (b) Distribution of leptons and jets p_T from the decay of a Z' produced at $\sqrt{s} = 10$ TeV with a mass of 9.5 TeV, as obtained at generator level. (c) p_T resolution for a muon track with $p_T = 5$ TeV as a function of the tracker radius (R_{max}) for different values of the detector magnetic field. (d) Minimum p_T required for a charged particle to reach the outermost tracker layer as a function of the magnetic field B for different tracker radius values (R_{max}). Figures taken from (68).

ventional. It is also important to ensure capability to study Higgs physics, as demonstrated with the $\sqrt{s} = 3$ TeV detector and predicted for $\sqrt{s} = 10$ TeV (Section 4). In the following, as for the case of 3 TeV center-of-mass energy, only one concept detector is discussed. The possibility to have two interaction points may lead to change the strategy in the future.

Figure 8a presents the b -quark p_T distributions from the $H \rightarrow b\bar{b}$ decays at $\sqrt{s} = 3$ and 10 TeV, as obtained at generator level with MadGraph5_aMC@NLO. Despite the higher center-of-mass energy, it is evident that the distributions are quite similar. Therefore the considerations made for Higgs physics at 3 TeV stand also at 10 TeV center-of-mass energy. It can be stated that Higgs physics lives in the low p_T regime even for the $\sqrt{s} = 10$ TeV muon collider. Another important feature is that Higgs bosons at $\sqrt{s} = 10$ TeV are emitted at smaller polar angles compared to 3 TeV, therefore the forward region of the detector should be designed carefully.

Going from the low energy regime to the high energy scale, **Figure 8b** shows the distributions of leptons and jets p_T from the decays of a Z' produced at $\sqrt{s} = 10$ TeV with a

mass of 9.5 TeV, as obtained at truth-level with MadGraph5_aMC@NLO: this distributions exhibit a peak at $p_T \sim 5$ TeV, and a long tail at lower p_T . A general consideration is that combinatorial and standard model backgrounds are expected to have a minor impact at high invariant mass compared to low invariant mass. It is crucial to maintain a good momentum resolution at low p_T , while at high p_T a moderate resolution should be sufficient.

5.2.1. Tracking system and magnetic field at $\sqrt{s} = 10$ TeV. The handles for improving the track momentum resolution are:

- Tracker transverse dimension.
- Number of tracking detector layers.
- Position resolution of the sensor.
- Magnetic field intensity.

To understand the possible tracker configurations, **Figure 8c** shows the p_T resolution as a function of the tracker radius (R_{max}) and magnetic field strength (B), as obtained by scaling analytically the detector's performance presented in **Section 3**. The curves are obtained with the same position resolution assumed for the $\sqrt{s} = 3$ TeV detector, as well as the number of tracking layers. The resolution on the hit position depends on the technology of the sensor, and various options have been explored for the muon collider experiment in (69).

The choice of the magnetic field is crucial: its magnitude determines the size, construction cost, operational cost, and the technological feasibility of the superconductive solenoid. As a rule of thumb, the energy density of the magnetic field is proportional to B^2 , and the solenoid cost has approximately the same scaling. Very high magnetic fields require the development of challenging technologies to maintain the mechanical and electrical stability of the superconducting coil, and obtain the uniformity of the field. For these reasons, it is important to aim for the lowest possible magnetic field strength, as long as it allows the desired physics performance to be achieved.

Increasing the magnetic field intensity enhances the tracking momentum resolution, but there is also a trade-off at low p_T : the minimum p_T required for a charged particle to reach the outermost layer of the tracker is proportional to B . In **Figure 8d** the minimum p_T as a function of B for different tracker radius hypotheses is shown. As an example, with $B = 5$ T and $R_{\text{max}} = 1.6$ m, the minimum p_T is 1.2 GeV. Below this threshold a deterioration of efficiency and/or resolution is expected. Preliminary results (68) indicate that going from $B = 3.57$ T to $B = 5$ T, assuming the detector configuration of **Section 3**, results in an efficiency loss of about 10% for reconstructing tracks originating from the $H \rightarrow b\bar{b}$ decay.

Based on the above considerations, a magnetic field strength between 4 and 5 T and a tracker radius larger than that of the $\sqrt{s} = 3$ TeV detector could be a good compromise at $\sqrt{s} = 10$ TeV. For instance, a radius of $R_{\text{max}} = 1.6$ m could be a suitable choice.

5.2.2. Calorimeter systems at $\sqrt{s} = 10$ TeV. Showers produced by photons, electrons, and hadrons with energies of the order of TeV need be contained in the calorimeters volume to achieve an adequate resolution on the energy measurement. For example, a photon with an energy of 1 TeV deposits less than 95% of its energy in 22 X_0 of ECAL (74), the depth of the electromagnetic calorimeter described in **Section 3**. The remaining energy spills into the HCAL. It is evident that the detector at $\sqrt{s} = 10$ TeV should have deeper calorimeters compared to the $\sqrt{s} = 3$ TeV configuration. Additionally, alternative materials with higher

X_0 values should be considered. In fact, it is important to remark that the dimensions of the detector are constrained by the cavern dimension, accelerator components, MDI and the magnet structure.

Another aspect to consider is the position of the solenoid with respect to the calorimeters. Placing the solenoid in front of the ECAL could shield the calorimeter from the low-energy BIB photons, but could also absorb the photons from $H \rightarrow \gamma\gamma$ with lower energies or the electromagnetic component of b -jets from $H \rightarrow b\bar{b}$, degrading the performance in the energy range where a precise resolution is crucial. On the other hand, positioning a high-field solenoid outside HCAL might be costly due to its large dimensions. A compromise could be placing the solenoid between ECAL and HCAL. However, defining the final configuration requires detailed simulation studies and the assessment of BIB impact.

Several calorimeter technologies that meet the requirements of a multi-TeV muon collider are currently under study. These technologies are not only being explored through simulations, but are also characterized with experimental tests. For examples, an ECAL made of PbF_2 crystals has been proposed (70), and the evaluation of Micro Pattern Gas detectors for the active layers of HCAL is ongoing (71).

5.2.3. Muon detection at $\sqrt{s} = 10$ TeV. Identifying and measuring muons with momenta in the TeV range present significant challenges. Promising technologies are discussed in (72), where gas detectors with excellent time resolution and high rate capability are presented. In the muon detector, the bending due to the residual magnetic field alone is not sufficient for the precise determination of muon p_T . Nevertheless, the muon detector can still be used to tag events with high momentum muons.

Additionally, high-granularity imaging calorimeters (77) could play an important role in detecting high-momentum muons since significant radiative losses are expected for these particles with p_T in the TeV range. Therefore, integrating information from all subsystems, including tracker, calorimeters and muon detectors, will be of paramount importance for muon reconstruction. It is essential to develop algorithms optimized for the TeV scale.

The detection of forward muons, *i.e.* muons that are scattered at very low angles with respect to the beam direction and pass through the nozzles, would be an important feature of the muon collider detector. This capability would make it possible to distinguish between the WW and $Z^0 Z^0$ fusion processes. The former is accompanied by forward neutrinos, while the latter has forward muons. At $\sqrt{s} = 10$ TeV, the muons from $Z^0 Z^0$ -fusion process are expected to be even more forward compared to $\sqrt{s} = 3$ TeV. Consequently, the detector acceptance may cover just a small fraction of the angular distribution. The feasibility of instrumenting the region close to the beam line to tag these muons is currently under investigation.

6. OUTLOOK

The muon collider facility, initially proposed by MAP, has been revised during the Accelerator R&D Roadmap (78) and by the IMCC, revealing no fundamental showstoppers. Using the same scheme as MAP for muon production, a preliminary design of a machine at a center-of-mass energy of 10 TeV was possible, opening up uncharted territory for lepton collisions.

For the first time, extensive studies have been conducted on detector performance in the presence of beam-induced background. Currently, the BIB simulation sample generated by

MAP is still used, due to the complexity of the generation process. Given the critical impact of BIB on the detector, extensive validations were done by using a different simulation software leading to consistent results. This validation gives confidence and robustness in the predictions of the beam-induced background. The proposed detector concept for $\sqrt{s} = 3$ TeV and the associated physics object reconstruction algorithms have demonstrated to be able to handle the effects of the beam-induced background, although neither the detector nor the algorithms have been optimized yet.

The physics performance assessed at $\sqrt{s} = 3$ TeV with the detailed detector simulation, including the effects of the beam-induced background, pertains mainly the Higgs physics. It was imperative to demonstrate that such a detector in such an environment has excellent capabilities to study an existing particle. Other studies are currently in development but have not yet been carried out due to lack of personnel.

Nonetheless, this has demonstrated that an initial stage of a muon collider operating at a center-of-mass energy of 3 TeV can achieve a performance comparable to that of the extensively studied CLIC detector at the same collision energy. While this energy is seen as the ultimate limit for e^+e^- colliders due to beamstrahlung radiation, it is considered the first stage for the muon collider.

The results obtained at $\sqrt{s} = 3$ TeV were used to benchmark parametric studies of the Higgs processes not included in the studies with the detailed detector simulation. Such studies were carried out at the same center-of-mass energy and at $\sqrt{s} = 10$ TeV and beyond. The possibility to reach high energy muon collisions allows to probe new physics by investigating various models including the precise determination of the Higgs potential.

A detector concept for muon collisions at 10 TeV center-of-mass energy is currently in preparation, the requirements were studied as discussed in this review for the first time. At $\sqrt{s} = 10$ TeV, the detector shielding structure needs to be designed, currently the nozzles optimized by MAP for $\sqrt{s} = 1.5$ TeV are used across all energies. Designing a new nozzle requires expertise that had been lost after MAP shutdown, only recently IMCC recovered it. Preliminary studies indicate that the amount of BIB particles arriving on the detector is not significantly larger than at $\sqrt{s} = 3$ TeV, the aim is to reduce the dimension of the tungsten material to enhance the detector acceptance in the forward region. This region is one of the open questions for a detector at muon collider. In fact, there are physics processes, as for example the Higgs physics, that at high energy, $\sqrt{s} \geq 10$ TeV, are produced with higher cross section in the forward region. It would be important to have at least the possibility to tag forward muons to distinguish between WW from Z^0Z^0 boson fusion production.

The design of the detector at $\sqrt{s} \geq 10$ TeV has demonstrated that the requirements for the technologies needed to achieve the desired performance could be satisfied through the R&D processes already ongoing for HL-LHC and future colliders. The muon collider community is actively engaged in the *Detector Research and Development collaborations - DRD* (79) in Europe and in the *Coordinating Panel for Advanced Detectors - CPAD* (80) in the United States. Participation in the development of new detector designs and related test beams for a novel detector concept is of crucial importance to engage and sustain the young community.

On a shorter time scale, the muon collider community may have to design and operate a facility to demonstrate the full muon ionization cooling chain. Experts in accelerator and detector technologies will need to collaborate together to address challenges previously not encountered. Moreover, both the detector R&D and the demonstration facility will play a vital role in actively involving the community in experimental activities, thereby preventing

the loss of valuable expertise and knowledge.

DISCLOSURE STATEMENT

The authors are not aware of any affiliations, memberships, funding, or financial holdings that might be perceived as affecting the objectivity of this review.

ACKNOWLEDGMENTS

We would like to thank the many people who contributed with their hard work, useful discussions, and valuable advice: Chiara Aimé, Paolo Andreetto, Nazar Bartosik, Laura Buonincontri, Daniele Calzolari, Luca Castelli, Giacomo Da Molin, Luca Giambastiani, Alessio Gianelle, Sergo Jindariani, Karol Kritza, Anton Lechner, Alessandro Montella, Mark Palmer, Simone Pagan Griso, Nadia Pastrone, Cristina Riccardi, Ilaria Vai, Davide Zuliani. We are grateful to the International Muon Collider Collaboration and the US Muon Accelerator Program for their support. We acknowledge the financial support of the Italian Institute for Nuclear Physics (INFN), the University of Padua, and the European Organization for Nuclear Research (CERN). This work was supported by the European Union's Horizon 2020 and Horizon Europe Research and Innovation programs through the Marie Skłodowska-Curie RISE Grant Agreement No. 101006726, the Research Infrastructures INFRADEV Grant Agreement No. 101094300, and the EXCELLENT SCIENCE - Research Infrastructures Research Innovation Grant Agreement No. 101004761.

LITERATURE CITED

1. Palmer M. In *Proceedings of the International Workshop on Beam Cooling and Related Topics*, Mürren, Switzerland, June 10-14, 2013. MOAM2HA02 <https://epaper.kek.jp/C00L2013>
2. Palmer M, Long K. *Muon Accelerators for Particle Physics (MUON)*, *J. Instrum. Special Issue* <https://iopscience.iop.org/journal/1748-0221/page/extraproc46>
3. The European Strategy Group. *Report* CERN-ESU-013-2020, Geneva, Switzerland (2020)
4. Snowmass 2021 Community. <https://snowmass21.org>
5. The International Muon Collider Collaboration. <https://muoncollider.web.cern.ch>
6. Accettura C, et al. *Eur. Phys. J. C* 83:864 (2023)
7. Bogomilov M, et al. (MICE Collab.) *Nature* 578:53 (2020)
8. Boscolo B et al. *Rev. Accel. Sci. Tech.* 10:189 (2019)
9. Cesarotti C, et al. *Phys. Rev. Lett.* 130:071803 (2023)
10. Han T, et al. arXiv:2205.11730 [hep-ph] (2022)
11. Black KM, et al. arXiv:2209.01318 [hep-ex] (2022)
12. Costantini A, et al. *J. High Energy. Phys.* 2020:80 (2020)
13. Mokhov NV, et al. arXiv:1202.3979 [physics.acc-ph] (2012)
14. Ginzburg IF. *Nucl. Phys. Proc. Suppl.* 51A:186 (1996)
15. Landau LD, Lifshitz EM. *Phys. Zs. Sovjet* 6:244 (1934)
16. Mokhov NV, Striganov SI. arXiv:1204.6721 [physics.ins-det] (2012)
17. Kahn SA, et al. In *Proceedings of the 2012 International Particle Accelerator Conference*, New Orleans, LA, USA, May 20-25, 2012. MOPPC038 <https://accelconf.web.cern.ch/ipac2012>
18. Mokhov NV, Striganov SI. *AIP Conf. Proc.* 896:50 (2007)
19. Mokhov NV, James CC. *Tech. Rep.* FERMILAB-FN-1058-APC, Fermi National Accel. Lab., Batavia, IL, USA (2017)
20. Collamati F, et al. *J. Instrum.* 16:P11009 (2021)

21. Ahdida C, et al. *Front. Phys.* 9:788253 (2022)
22. Mereghetti A, et al. In *Proceedings of the 2012 International Particle Accelerator Conference*, New Orleans, LA, USA, May 20-25, 2012. WEPPD071 <https://accelconf.web.cern.ch/ipac2012>
23. Agostinelli S, et al. *Nucl. Instrum. Methods A* 506:250 (2003)
24. Alexahin Y, et al. *J. Instrum.* 13:P11002 (2018)
25. Calzolari D, et al. In *Proceedings of the 14th International Particle Accelerator Conference*, Venice, Italy, May 7-12, 2023. MOPA090 <https://accelconf.web.cern.ch/ipac2023>
26. Calzolari D, Skoufaris K. *Proc. Sci.* ICHEP2022:063 (2023)
27. The International Linear Collider. <https://linearcollider.org>
28. The Compact Linear Collider. <https://clic.cern>
29. The Future Circular Collider. <https://fcc.web.cern.ch>
30. The Circular Electron Positron Collider. <http://cepc.ihep.ac.cn>
31. Evans L, Bryant P. *J. Instrum.* 3:S08001 (2008)
32. Aberle O, et al. *Yellow Report* CERN-2020-010, CERN, Geneva, Switzerland (2020)
33. Lamont M. *J. Phys.: Conf. Ser.* 455:012001 (2013)
34. Aad G, et al. (ATLAS Collab.) *J. Instrum.* 3:S08003 (2008)
35. Chatrchyan S, et al. (CMS Collab.) *J. Instrum.* 3:S08004 (2008)
36. Alipour Tehrani N, et al. *Note CLICdp-Note-2017-001*, CERN, Geneva, Switzerland (2017)
37. Muon Collider Software framework. <https://github.com/MuonColliderSoft>
38. iLCSoft framework. <https://ilcsoft.desy.de/portal>
39. Frank M, Gaede F, Grefe C, Mato P. *J. Phys. Conf. Ser.* 513:022010 (2014)
40. Kilian W, Ohl T, Reuter J. *Eur. Phys. J. C* 71:1742 (2011)
41. Alwall J, et al. *J. High Energy Phys.* 2014:79 (2014)
42. Marlin framework. <https://github.com/iLCSoft/Marlin>
43. Billoir P, Qian S. *Nucl. Instrum. Methods A* 294:219 (1990)
44. Thomson MA. *Nucl. Instrum. Methods A* 611:25 (2009)
45. Catani S, Dokshitzer YL, Seymour MH, Webber BR. *Nucl. Phys. B* 406:187 (1993)
46. Ellis SD, Soper DE. *Phys. Rev. D* 48:3160 (1993)
47. Da Molin G. Study of b - and c - jets identification for Higgs coupling measurement at muon collider. Master's Thesis, Univ. of Padua, Padua, Italy (2021)
48. Aad G, et al. (ATLAS Collab.) arXiv:2212.09379 [hep-ex] (2022)
49. Abudinén F, et al. (BelleII Collab.) *Chinese Phys. C* 44:021001 (2020)
50. van der Meer S. *Report* CERN-ISR-PO-68-31, CERN, Geneva, Switzerland (1968)
51. Calame C, et al. *Nucl. Phys. B Proc. Suppl.* 225-227:293 (2012)
52. Giraldin C, et al. *Proc. Sci.* LHCP2021:341 (2021)
53. Sjöstrand T, et al. *Comput. Phys. Commun.* 191:159 (2015)
54. Ambrosino F, et al. (KLOE Collab.) *Eur. Phys. J. C* 47:589 (2006)
55. Workman RL, et al. *Prog. Theor. Exp. Phys.* 2022:083C01 (2022)
56. Ali HA, et al. *Rep. Prog. Phys.* 85:084201 (2022)
57. Abramowicz H, et al. *Eur. Phys. J. C* 77:475 (2017)
58. Buonincontri L. Study of mitigation strategies of beam-induced background and Higgs boson couplings measurements at a muon collider. Master's Thesis, Univ. of Padua, Padua, Italy (2020)
59. Castelli L. Study of $H \rightarrow WW$ reconstruction and coupling precision determination at Muon Collider. Master's Thesis, Univ. of Padua, Padua, Italy (2022)
60. Sestini L, et al. *Proc. Sci.* ICHEP2022:515 (2023)
61. Casarsa M, et al. *Proc. Sci.* EPS-HEP2023:408 In press
62. Montella A. Study of the Physics Potential of the $H \rightarrow \mu\mu$ Direct Decay Channel at a 3 TeV Muon Collider. Master's Thesis, Univ. of Trieste, Trieste, Italy (2021)
63. David A, et al., arXiv:1209.0040 [hep-ph] (2012)

64. Forslund M, Meade P. *J. High Energ. Phys.* 2022:185 (2022)
65. Han T, Liu D, Low I, Wang X. *Phys. Rev. D* 103:013002 (2021)
66. Chiesa M, et al. *J. High Energ. Phys.* 2020:98 (2020)
67. De Blas J, et al. arXiv:2203.07261 [hep-ph] (2022)
68. Sestini L, et al. *Proc. Sci.* EPS-HEP2023:552 In press
69. Jindariani S et al. arXiv:2203.07224v1 [physics.ins-det] (2022)
70. Ceravolo S, et al. *J. Instrum.* 17:P09033 (2022)
71. Aruta C, et al. *Nucl. Instrum. Methods A* 1047:167731 (2023)
72. Aimé C, et al. *Nucl. Instrum. Methods A* 1046:167800 (2023)
73. Capdevilla R, Meloni F, Simoniello R, Zurita J. *J. High Energ. Phys.* 06:133 (2021)
74. Aleksa M, et al. arXiv:1912.09962 [physics.ins-det] (2019)
75. Han T, Liu Z, Wang LT, Wang X. *Phys. Rev. D* 103, 075004 (2021)
76. Casarsa M, Fabbrichesi M, Gabrielli E. *Phys. Rev. D* 105:075008 (2022)
77. Bilki B et al. [CALICE], *J. Phys. Conf. Ser.* 2374 (2022) no.1, 012022
78. CERN Yellow report, <https://doi.org/10.23731/CYRM-2022-001>
79. The CERN Scientific Policy Committee. *Report* CERN/SPC/1190, CERN, Geneva, Switzerland (2022)
80. The Coordinating Panel for Advanced Detectors. <https://cpad-dpf.org>